Generation of Fiber-Coupled, Nondegenerate, Polarization-Entangled Photons for Quantum Communication

by

ARCHIVES

Bhaskar Mookerji

Submitted to the Department of Physics
in partial fulfillment of the requirements for the degree of

Bachelor of Science in Physics

at the

MASSACHUSETTS INSTITUTE OF TECHNOLOGY

June 2009

© Massachusetts Institute of Technology 2009. All rights reserved.

Author ....
Department of Physics
May 22, 2009

Certified by. ....
Franco Wong
Senior Research Scientist
Thesis Supervisor

Accepted by ....
David E. Pritchard
Senior Thesis Coordinator

MASSACHUSETTS INSTITUTE OF TECHNOLOGY
JUL 0 7 2009
LIBRARIES

Generation of Fiber-Coupled, Nondegenerate, Polarization-Entangled Photons for Quantum Communication

by

Bhaskar Mookerji

Submitted to the Department of Physics
on May 22, 2009, in partial fulfillment of the
requirements for the degree of
Bachelor of Science in Physics

Abstract

The production of polarization-entangled photon pairs from spontaneous parametric downconversion (SPDC) enables many applications of quantum information processing. In this thesis, we use type-0 phase-matched downconversion of pump photons from a 532 nm continuous-wave laser to generate 798 nm signal and 1.6 μm idler photon pairs in periodically-poled, congruent lithium niobate (PPLN). Difference frequency generation of 798 nm is used for characterizing PPLN, including phase matching bandwidth and effective nonlinear coefficient. Optimal focusing for generating a single spatial mode SPDC output allows efficient coupling of signal and idler photons. Through coincidence counting, our source's spectral brightness is measured to be 3.6×10^5 Hz/mW/nm detected pairs/s/mW of pump power per nm of output photon bandwidth with an idler conditional detection efficiency of 1.6%. This work is a significant first step toward realizing a high-flux source of nondegenerate polarization-entangled photons.

Thesis Supervisor: Franco Wong
Title: Senior Research Scientist

We often discussed his notions on objective reality. I recall that during one walk Einstein suddenly stopped, turned to me and asked whether I really believed that the moon exists only when I look at it. The rest of this walk was devoted to a discussion of what a physicist should mean by the term “to exist.”

— Abraham Pais, *Einstein and the quantum theory* [Pai79]

Acknowledgments

My first gratitude for the completion of this work goes to Franco Wong, my thesis supervisor and principal of the Quantum and Optical Communications Group's experimental program. Clever, supportive, thoughtful, and grounded, Franco has been a fantastic supervisor, always leading me through my frustrations with practical optics and being supportive despite my many difficulties. Nonlinear optics is a great test bed and tool for experimental quantum information, as the qubits stay around long enough to be appreciated. I hope more undergraduates find their way to Franco with interests in this area.

Quantum mechanics is a beautiful subject, an elegant theory contributing not only to our understanding of matter and the nature of fundamental interactions, but also to a technological abundance far beyond its creators' dreams. I also thank my teachers in this subject, particularly Jeff Shapiro, for my first thorough introduction to the theories of quantum information and quantum optics. Jeff's quantum optical communications class (6.453) was a fantastic synthesis of quantum optics and systems analysis, taught with the practical eye of an engineer.

I also thank Franco's graduate students, Tian Zhong and Dheera Venkatraman, and his post-doc Julien LeGouet, who have also been helpful and supportive when help was needed. Dheera was a wellspring of information, having used my crystal source to carry out similar experiments in the past. Tian and Julien are particularly gifted teachers of practical optics, and I hope they have opportunities to support more undergraduate thesis students in the future.

Of course, none of this have been possible without the help of my parents, Dipankar and Mallika Mookherji, to whom this thesis is dedicated. Their great courage in coming to the United States has provided me unparalleled opportunities to learn and grow without worry. Their support, as well as the help from my friends, PP, MT, MG, CH, JT, and MP, has carried me to this finish line.

Funding for this project during the Fall 2008 term was provided by the Paul Gray Undergraduate Research Opportunities Program (UROP) fund.

Contents

1 Introduction **13**

1.1 Polarization Entangled Bell States and Applications 13

1.2 Photonic Entanglement Sources 15

1.3 Overview and Goals 17

1.4 Notation and Abbreviations 18

2 Nonlinear Optics and Spontaneous Parametric Downconversion **19**

2.1 $\chi^{(2)}$ Nonlinear Optical Processes 19

2.2 Phase Matching 21

2.3 Parametric Downconversion in Periodically Polled Crystals 24

2.4 Optimal Focusing of Entangled Photon Pairs 25

2.5 Summary 26

3 Experimental Design and Results **27**

3.1 Experimental Setup for Difference Frequency Conversion 28

3.2 Phase Matching Bandwidth 31

3.3 Effective Nonlinear Coefficient 33

3.4 SPDC Flux of Single Photons 35

3.5 Coincidence Counting in a Single-Pass Measurement 38

3.6 Summary 41

4 Conclusion **43**

A Mode Matching Gaussian Laser Beams **45**
A.1 Gaussian Beam Propagation 45
A.2 Mode Matching With a Single Thin Lens 46

List of Figures

1-1 Comparing entanglement sources with different designs [KMW$^+$95, KWW$^+$99, KFW06, FMK$^+$04, KOW01]. Figure taken from the Ph.D thesis of Taeyhum Kim [Kim08]. 16

2-1 Schemes and efficiencies for phase matching with second-harmonic generation. Figure 2-1(a) shows how birefringence of ordinary (o) and extraordinary (e) waves achieves critical phase matching at angular adjustment θ from optic axis z. Figure 2-1(b) compares non-phase matched (η_{NPM}), quasi-phase matched (η_{QPM}), and ideally phase-matched (η_{PM}) conversion efficiencies, where l_c is the coherence length [BZ06]. 22

2-2 Spontaneous parametric down conversion at 810 and 1550 nm. Photons from nondegenerate cones (e and o polarized) are collected along directions labeled 1 and 2. A similar figure is found in [dCSS$^+$06]. . . 24

3-1 Temperature and wavelength tuning behavior for quasi-phase matching. By choosing a correct temperature and grating, we can achieve quasi-phase matching by tuning signal wavelength. 28

3-2 Schematic difference frequency generation setup. 29

3-3 Phasematching and temperature bandwidth measurement and theory for 7.2 μm grating in 20 mm PPLN crystal. Figures 3-3(a) and 3-3(b) show experimental and generated phase matching curves for PPLN, their Gaussian fits, and the residuals. Comparing their fits, we see that a shorter effective crystal length is required to explain experimental phase matching and temperature bandwidths. 32

3-4 Linear dependence of difference frequency generation at 797 nm on signal power 1.6 μm at 532 nm fixed pump. 34
3-5 Coincidences versus signal-idler time-bin delay. 38
3-6 Conditional coincidence counting of idler photons. 39

A-1 Mode matching with a single thin lens and coupling into single-mode optical fiber. 47

List of Tables

1.1 Common symbols and abbreviations referenced in this thesis. 18

3.1 Sellmeier and thermal expansion coefficients for 20mm PPLN crystal sample 28

Chapter 1

Introduction

Experimental quantum information science applies quantum mechanical resources, such as entanglement, to practical engineering applications in physical communication, computation, and metrology, often providing advantages unrealizable by their classical counterparts. A representative physical carrier for a quantum bit ('qubit') is the photon, which experiences only weak decoherence and interaction with its environment. The weak attenuation of photons through single-mode optical fibers allows the transfer of photonic qubits over long distances (e.g., kilometers), including the establishment of two-qubit entanglement for quantum key distribution (QKD). In the following introduction, we will relate the context of these applications to the work described in this thesis.

1.1 Polarization Entangled Bell States and Applications

Entangled quantum states are a singular example of Nature deviating from our classical perception of reality. Albert Einstein, along with Boris Podolski and Nathan Rosen, argued that the behavior of entangled quantum states defied classical intuition, and subsequently questioned the quantum mechanical description of nature [EPR35]. However, experiments with these Einstein-Podolsky-Rosen (EPR) states validated such strange behavior, showing that classical intuition was actually at fault. John Bell later proved that the correlations produced from measuring entangled states distinctly surpassed those measured with classical light [Bel]. We now know that the correlation from entanglement is useful in a variety of practical applications, such as precision measurement beyond the capabilities of classical light [AAS+02], increased communications rates through noisy channels [BW92], teleportation of quantum states [BBC+93, BPM+97], and the exponential speedup of certain computational problems [EJ96].

Linear optical systems can be used to manipulate elements of an entangled basis. A two-mode state of light $|\psi\rangle_{\mathrm{AB}}$ of a composite system is considered entangled if and only if there do not exist $|\psi\rangle_{\mathrm{A}}$ and $|\psi\rangle_{\mathrm{B}}$ such that

$$|\psi\rangle_{\mathrm{AB}} = |\psi\rangle_{\mathrm{A}} \otimes |\psi\rangle_{\mathrm{B}}\,, \tag{1.1}$$

where $\otimes$ is the tensor product of the Hilbert spaces $\mathcal{H}_{\mathrm{A}} \otimes \mathcal{H}_{\mathrm{B}}$. To date, optically entangled quantum states have been produced using a second-order nonlinear process known as spontaneous parametric down conversion (SPDC), where a pump photon incident on a birefringent crystal is split into correlated signal and idler pairs of parallel (type I) or orthogonal (type II) polarizations. For example, two type-I phase-matched crystals crystals arranged with orthogonal orientations can yield a polarization-entangled state given by

$$|\psi\rangle = \frac{1}{\sqrt{2}} \left(|H\rangle_s |H\rangle_i + e^{j\phi} |V\rangle_s |V\rangle_i \right), \tag{1.2}$$

where $|H\rangle$ and $|V\rangle$ denote horizontal (H) and vertical (V) polarization states and ϕ is a relative phase [KWW+99]. The photons from this process can be separated using linear optical components, such as a dichroic beam splitter. The presence of a birefringent phase shifter, such as a half-wave plate (HWP) in the path of one photon, can alter ϕ and produce any one of four polarization-entangled EPR-Bell states,

$$|\psi^{\pm}\rangle = \frac{1}{\sqrt{2}}\left(|H\rangle_s|V\rangle_i \pm |V\rangle_s|H\rangle_i\right) \quad \text{and} \quad |\phi^{\pm}\rangle = \frac{1}{\sqrt{2}}\left(|H\rangle_s|H\rangle_i \pm |V\rangle_s|V\rangle_i\right), \tag{1.3}$$

which form an entangled basis set in a two-qubit Hilbert space.

1.2 Photonic Entanglement Sources

SPDC in a nonlinear crystal converts a single pump photon (**p**) into a pair of subharmonic photons (labelled signal **s** and idler **i**) while maintaining momentum and energy conservation such that $\mathbf{k}_p = \mathbf{k}_s + \mathbf{k}_i$ and $\omega_\mathbf{p} = \omega_\mathbf{s} + \omega_\mathbf{i}$. Crystal choice and optical configurations can be tailored to yield a source of entangled photons with desirable parameters such as wavelength, flux, bandwidth, and type of entanglement. For example, momentum conservation of pump, signal, and idler photons (also known as phase matching) is temperature dependent, and for a given emission angle, restricts the creation of wavelength-degenerate photons to a particular temperature. Quasi-phase matching solves this problem by periodically inverting the crystal's effective nonlinearity with an alternating electric field during fabrication, thus creating a grating that allows phase matching at user-defined wavelengths. This process eases the requirements for phase-matching angles and wavelengths that would otherwise be impossible if angle and birefringence phase-matching were the only methods available.

The creation of polarization-entangled photon pairs by SPDC is an example of a second-order nonlinear optical effect. An intense electric field is required to overcome the electrostatic interaction between an electron and an atomic nucleus, which is on the order of 10^9 V/m. Typical point light sources yield electric fields below 10^2 V/m, inducing only linear polarization responses, whereas focused laser beams can apply fields on the order of 10^7 V/m. Because of the inefficiency of such higher order processes, the construction of SPDC sources focuses on increasing flux and entanglement quality of correlated pairs.

Efficient quantum information processing requires a high-flux SPDC source with

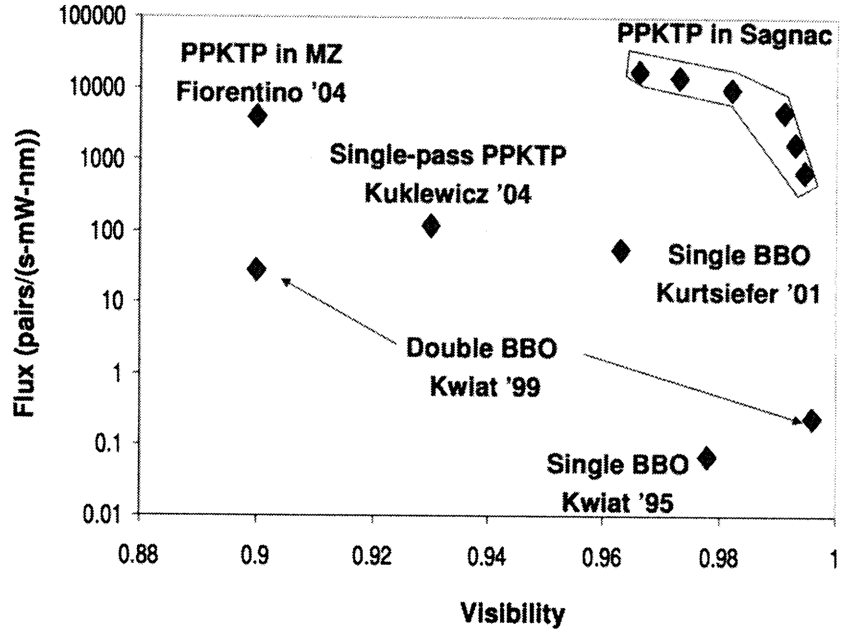

Figure 1-1: Comparing entanglement sources with different designs [KMW+95, KWW+99, KFW06, FMK+04, KOW01]. Figure taken from the Ph.D thesis of Taeyhum Kim [Kim08].

excellent entanglement quality, and Figure 1-1 compares entanglement sources with different configurations and phase matching. Figure 1-1 parametrizes such sources with two parameters measured through coincidence experiments. The first is spectral brightness (flux of coincident photons per unit pump power and bandwidth), and the second is entanglement fidelity, a measure of the statistical correlation between signal and idler photons when projected onto a diagonal basis ($|D\rangle$ and $|A\rangle$). Paul Kwiat *et al.* constructed the first high-quality sources using single and double beta barium borate (BBO) crystals with type-II and type-I phase matching, respectively [KMW+95, KWW+99]. These SPDC sources were limited by spatial-mode distinguishability and small crystal length, thus limiting its useful output flux. Later SPDC sources allowed a significantly larger output SPDC flux to be collected by using doubly and bidirectionally pumped configurations [KFW06, FMK+04, KOW01]. The first of these interferometrically combined the outputs of two downconverters with a polarizing beampsplitter, first in a single-pass measurement, and then in a Mach-Zehnder interferometer. This latter configuration was inherently sensitive to vibrations and required active phase stabilization of one interferometer path to achieve a high visibility. Shi and Tomita avoided active stabilization by using an inherently phase-stable Sagnac interferometer and a type-I BBO crystal [ST04]. Recent work in our group dramatically improved the yield of output flux and visibility by combining the phase stable configuration of a Sagnac interferometer with a bidirectionally pumped type-II potassium titanyl phosphate (PPKTP) crystal [KFW06].

1.3 Overview and Goals

The aim of this thesis project is to construct an SPDC source with a periodically-poled, congruent lithium niobate (PPLN) that is spectrally bright and suitable for use in long-distance quantum communication. The discussion in this thesis starts with the basics of nonlinear optics applied to spontaneous parametric downconversion, and concludes with the construction and evaluation of a fiber-coupled source of nondegenerate, SPDC signal and idler photons.

The chapter contents are as follows:

- **Chapter 2** describes some basic facts about nonlinear optics and SPDC. Section 2.1 introduces nonlinear polarization response and the second-order susceptibility tensor for PPLN. Section 2.3 discusses the production of polarization-entangled photons and SPDC's spatial mode structure, and Section 2.2 discusses the efficiency of this process when phase matching with spatially modulated nonlinearities is used. Section 2.4 applies our discussion of the mode structure from SPDC to the problem of coupling to a single-mode optical fiber.

- **Chapter 3** summarizes our experimental evaluation of a quasi-phase matched PPLN crystal as a source for nondegenerate polarization entangled photons. Sections 3.1, 3.2, and 3.3 apply a DFG process to evaluate the phase matching and temperature bandwidth of PPLN. In Section 3.4 and 3.5, we setup a single-pass SPDC measurement, evaluate its single-mode fiber coupling, and measure the pair generation rate through coincidence counting with single photon de-

Symbol/Abbreviation	Definition
	Symbols
k	Momentum wavenumber given by $2\pi n/\lambda$
w_0	Gaussian beam waist
b, z_R	Confocal parameter, Rayleigh range
P	Power
l	Physical crystal length
ξ	Focusing parameter given by l/b
	Nonlinear Optics
SPDC	Spontaneous parametric down conversion
EPR	Einstein-Podolsky-Rosen
DFG	Difference frequency generation
PPLN	Periodically poled lithium niobate ($LiNbO_3$)
OPA	Optical parametric amplification
	Hardware
Si/InGaAs	Silicon/Indium gallium arsenide
SPCM	Single photon counting module
HWP/QWP	Half-/Quarter-wave plate
PBS	Polarizing beam splitter
AR	Anti-reflection
HT/HR	Highly transmissive, highly reflective

Table 1.1: Common symbols and abbreviations referenced in this thesis.

tectors.

- **Chapter 4** concludes with a discussion of our experimental results, related research by other groups, and prospects for future experiments.

- **Appendix A** describes the propagation and transformation of laser beams with Gaussian intensity profiles. Section A.1 parametrizes the free-space propagation of a Gaussian beam. Section A.2 summarizes the mode matching of Gaussian beams between two optical structures with a single thin lens and its application to coupling laser light into a single-mode optical fiber.

1.4 Notation and Abbreviations

Table 1.1 summarizes symbols and abbreviations common throughout this thesis.

Chapter 2

Nonlinear Optics and Spontaneous Parametric Downconversion

Nonlinear optical devices, such as optical parametric oscillators and harmonic generators, extend the frequency of laser sources by using the nonlinear optical response of birefringent materials in the presence of intense electric fields. This chapter describes basic aspects of nonlinear optics relevant to understanding the production of polarization-entangled photon pairs through SPDC. The results will be discussed in the context of PPLN.

2.1 $\chi^{(2)}$ Nonlinear Optical Processes

We will analyze nonlinear optical effects by considering the response of a dielectric material to the electric fields of an intense light beam. Consider z-propagating plane wave solutions to Maxwell's Equations in the frequency domain,

$$\mathcal{E}\left(z,\omega\right) = \mathrm{Re}\left[\mathbf{E}e^{-j(\omega t - kz)}\right] \tag{2.1}$$

incident on the entrance face ($z = 0$) of a crystalline material. Recall that the induced polarization response per unit volume $\mathcal{P}$ in this material is dependent on the magnitude of the applied electric field $\mathcal{E}$. Relatively weak electric fields can cause atoms in a crystal to become polarized, inducing a macroscopic charge polarization in a linear material. The constitutive law for a linear dielectric medium is given by

$$\mathcal{D}(z,\omega) = \epsilon_0 \left[1 + \chi^{(1)}(\omega)\right] \mathcal{E}(z,\omega) = \epsilon_0 \mathcal{E}(z,\omega) + \mathcal{P}_{\mathrm{L}}(z,\omega), \tag{2.2}$$

where $\chi^{(1)}(\omega)$ is a frequency dependent tensor characterizing linear susceptibility. An assumption of this semi-classical model is that at low powers, electrons in a medium will act as harmonic oscillators with a constant spring coefficient $\epsilon_0\chi^{(1)}(\omega)$. At higher powers however, the polarization response of the medium can be expanded in a power series of electric field amplitudes,

$$\mathcal{P} = \epsilon_0 \left(\chi^{(1)}(\omega)\mathcal{E} + \chi^{(2)}\mathcal{E}^2 + \chi^{(3)}\mathcal{E}^3 + \cdots\right) \tag{2.3}$$

with the resulting dielectric field response

$$\mathcal{D}(z,\omega) = \epsilon_0 \mathcal{E}(z,\omega) + \mathcal{P}_{\mathrm{NL}}(z,\omega). \tag{2.4}$$

By substituting this constitutive law for the nonlinear dielectric medium into Maxwell's Equations, it can be shown that the electric field within the crystal of refractive index n is given by

$$\left(\frac{\partial^2}{\partial z^2} + \frac{\omega^2 n^2(\omega)}{c^2}\right)\mathcal{E}(z,\omega) = -\mu_0\omega^2\mathcal{P}_{\mathrm{NL}}(z,\omega). \tag{2.5}$$

The left-hand side of this expression includes the linear behavior of the medium, while right-hand side is a nonlinear driving term that can deliver power to or remove power from the field $\mathcal{E}(z,\omega)$ depending on the relative phase of $\mathcal{E}(z,\omega)$ and $\mathcal{P}_{\mathrm{NL}}(z,\omega)$.

By substituting a field $\mathcal{E}(z,\omega)$ of sum of three-waves (pump, signal, and idler) into Equation 2.5, it can be shown that the second-order susceptibility $\chi^{(2)}$ gives rise to a variety of second harmonic generation, sum and difference frequency generation, and spontaneous parametric downconversion. The second-order polarization response in Cartesian coordinates is given by,

$$\mathcal{P}_i^{(2)}(z,\omega) = \epsilon_0\chi_{ijk}^{(2)}\mathcal{E}_j(z,\omega)\mathcal{E}_k(z,\omega) \qquad (i,j,k = 1,2,3), \tag{2.6}$$

where $\chi^{(2)}_{ijk}$ is a second-order susceptibility tensor with 27 independent constants, denoted as d_{ijk} in the engineering literature. Under symmetry constraints of Equation 2.6, this term is expressed by a 3 × 6 matrix. The algebraic symmetry group of the crystal reduces the number of possible nonlinear polarizations allowed. PPLN belongs to the trigonal symmetry class 3m-C_{3v} and has the tensor

$$d_{ijk} = \begin{bmatrix} 0 & 0 & 0 & 0 & d_{15} & -d_{22} \\ -d_{22} & d_{22} & 0 & d_{15} & 0 & 0 \\ d_{31} & d_{31} & d_{33} & 0 & 0 & 0 \end{bmatrix}. \tag{2.7}$$

By specifying the polarizations of the interacting fields along the principal axes of the crystal, we can replace $d^{(2)}_{ijk}$ by an effective scalar nonlinear coefficient d_{eff} proportional to the matrix element of our choice. This process, however, is constrained by our choice of phase matching, as described in the next section.

2.2 Phase Matching

Phase-sensitive nonlinear processes, such as second harmonic generation, difference frequency generation, and spontaneous parametric downconversion, require phase matching to be efficient. Recall that a wave propagating with frequency ω through a dispersive medium with refractive index $n(\omega)$ has a phase velocity $v = \omega/k$, where k is its wavevector. Any three-wave mixing process with pump, signal, and idler fields at wavelengths λ_p, λ_s, and λ_i satisfies energy conservation such that

$$\omega_p = \omega_s + \omega_i, \tag{2.8}$$

but will experience a phase mismatch

$$\begin{aligned} \Delta k &= k_p - k_s - k_i \\ &= n_p(\lambda_p)\frac{2\pi}{\lambda_p} - n_s(\lambda_s)\frac{2\pi}{\lambda_s} - n_i(\lambda_i)\frac{2\pi}{\lambda_i} \end{aligned} \tag{2.9}$$

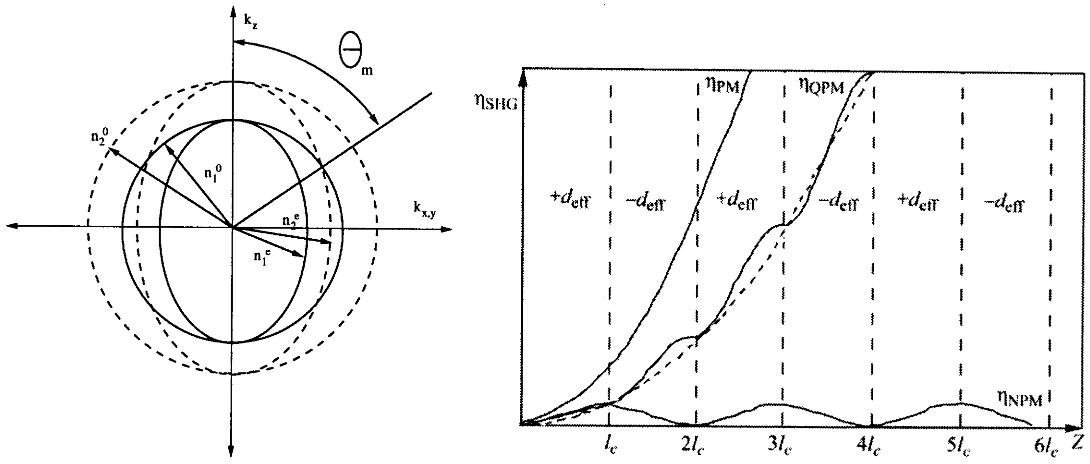

(a) Cross-sectional dispersion relations for birefringent phase matching at two wavelengths.

(b) Conversion efficiencies for SHG.

Figure 2-1: Schemes and efficiencies for phase matching with second-harmonic generation. Figure 2-1(a) shows how birefringence of ordinary (o) and extraordinary (e) waves achieves critical phase matching at angular adjustment θ from optic axis z. Figure 2-1(b) compares non-phase matched (η_{NPM}), quasi-phase matched (η_{QPM}), and ideally phase-matched (η_{PM}) conversion efficiencies, where l_c is the coherence length [BZ06].

due to the differing phase velocities amongst the three waves. This phase mismatch term Δk defines a coherence length $l_c = \pi/\Delta k$ during which the relative phase between the waves shifts by π radians, causing an alternation in the flow of power between the pump and signal/idler waves. This alternation in the power creates a repetitive growth and decay of conversion efficiency, as show in Figure 2-1, over the length of the interaction. If the phase matching condition $\Delta k = 0$ is met, then the conversion intensity will grow monotonically through the crystal.

In terms of refractive indices $n(\omega)$, the collinear phase matching condition $\Delta k = 0$ can be written as,

$$\omega_s \left[n_p(\omega_p) - n_s(\omega_s)\right] + \omega_i \left[n_p(\omega_p) - n_i(\omega_i)\right] = 0. \tag{2.10}$$

Isotropic cubic materials with refractive indices $n(\omega_p) > n(\omega_s), n(\omega_i)$ can never satisfy this dispersion relation. However, waves propagating in negative uniaxial crystals experience birefringence, decomposing into ordinary (o) and extraordinary (e) waves with wavevectors $\mathbf{k}_o$ and $\mathbf{k}_o$, respectively. For each wave in birefringent crystal, $n_e(\omega) < n_o(\omega)$, and it is therefore possible to find a choice of input frequencies, input polarizations, and propagation axes such that the phase matching condition is met. Figure 2-1(a) shows a cross-section of the dispersion relations for the ordinary and extraordinary waves in a negative uniaxial medium. The phase matching condition is satisfied for a crystal offset by an angle θ_m from the optical z-axis.

Figure 2-1(b) shows an alternative method of achieving this condition known as quasi-phase matching. This technique periodically resets the relative phases between the pump and signal/idler waves, thereby allowing a coherent phase relationship for generation efficiency. QPM eases the requirements for perfect phase matching by adding to Equation 2.9 a compensating term such that

$$\Delta k = k_p - k_s - k_i - \frac{2\pi}{\Lambda}, \tag{2.11}$$

where $\Lambda = 2l_c$ is the grating period. This term repeatedly resets the relative phase between the three waves every odd-number m of coherence lengths l_c by inverting the sign of the nonlinear coefficient. The efficiency of these interactions with QPM is directed related to the effective nonlinear coefficient

$$d_m = \frac{2}{m\pi} \sin(m\pi D)\, d_{\text{eff}}, \tag{2.12}$$

where D is the grating duty cycle, m is the order of the QPM grating, and d_{eff} is the nonlinear coefficient at perfect birefringent phase matching [FMJB92]. For a first-order grating ($m = 1$) and $D = 0.5$, the resulting nonlinear efficient is given by $d_{\text{eff}} = 2d_{33}/\pi$. Because QPM frees our choice of three-wave polarizations, we can choose a larger nonlinear coefficient from Equation 2.7. For example, d_{33} is often chosen in PPLN because it is five times larger than d_{31}. For d_{33}, the pump, signal, and idler fields have the same polarization along the crystal's z-axis, which is termed type-0 phase matching.

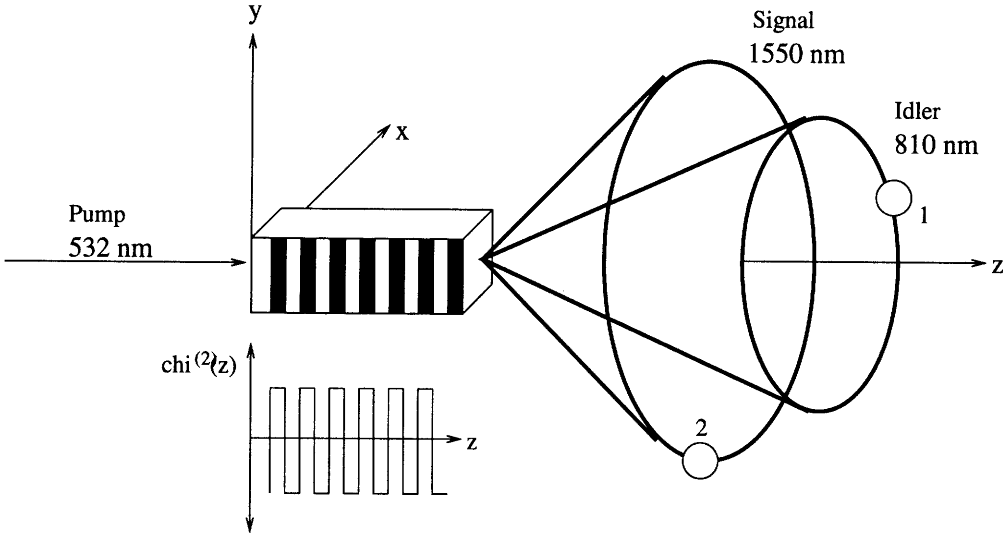

Figure 2-2: Spontaneous parametric down conversion at 810 and 1550 nm. Photons from nondegenerate cones (*e* and *o* polarized) are collected along directions labeled 1 and 2. A similar figure is found in [dCSS+06].

2.3 Parametric Downconversion in Periodically Polled Crystals

A powerful tool for generating polarization entangled Bell states described in Equation 1.3 is spontaneous parametric down conversion (SPDC). In this process (shown in Figure 2-2), a beam of coherent radiation (called the pump) is incident on a birefringent crystal, and the electromagnetic field of a single photon interacts with the atoms of the medium via absorption. The nonlinear polarization response converts higher energy near-ultraviolet pump photons into near-infrared and infrared pairs of correlated photons (called signal and idler, respectively). The phase matching process can be either type-I or type-II, depending on whether the output photons have parallel or orthogonal polarizations. In addition, type-0 phase matching refers to the case that all these fields are co-polarized.

When the phase matching condition is met, the process of spontaneous parametric downconversion is quantified by the interaction Hamiltonian

$$\hat{H} = \kappa \left(\hat{a}_s^\dagger \hat{a}_i^\dagger \hat{a}_p + \hat{a}_s \hat{a}_i \hat{a}_p^\dagger \right), \tag{2.13}$$

which describes the coupling (with constant κ) of pump, signal, and idler waves as modes of a quantized electromagnetic field—$\hat{a}_p$, $\hat{a}_s$, and $\hat{a}_i$, respectively. In this interaction picture, a pump photon is annihilated and signal/idler photons are created, and vice versa. The coupling constant κ is small, as the SPDC interaction is a second-order process. The pump field $\mathcal{E}_p$ is well approximated by a classical coherent state due to the large number of pump photons. As such, we can replace $\hat{a}_p$ with the complex amplitude α_p of the corresponding coherent state. In the interaction picture under the classical pump approximation, SPDC is well described by the unitary squeezing operator

$$\hat{S} = \exp \left[-j\kappa t \left(\alpha_p \hat{a}_s^\dagger \hat{a}_i^\dagger + \alpha_p^* \hat{a}_s \hat{a}_i \right) \right] \tag{2.14}$$

applied to the vacuum state $|0\rangle_s |0\rangle_i$, yielding

$$\hat{S} |0\rangle_s |0\rangle_i = \frac{1}{\cosh(\kappa t)} \sum_{n=0}^{\infty} (\kappa t)^n |n\rangle_s |n\rangle_i . \tag{2.15}$$

Because κ is small, the vast majority of $\hat{S} |0\rangle_s |0\rangle_i$ remains in the vacuum state, with a small probability for the desired bi-photon state. As shown in Figure 2-2, the phase matching condition restricts the transverse emission of k vectors for signal and idler photon pairs.

2.4 Optimal Focusing of Entangled Photon Pairs

The multiple spatial modes generated in SPDC complicate the efficient coupling of entangled photons into single-mode optical fibers, a necessary step for long-distance quantum communication. As described in Appendix A, an idealized single-mode optical fiber can only couple a single spatial mode, and only at optimal efficiency when properly mode matched. SPDC does not generally produce single spatial modes in either the signal or idler photons, and will subsequently lead to poor coupling efficiency.

Several authors have investigated the maximum achievable coupling of signal and idler photons in crystals phase matched for collinear emission [BLEG06, LT05]. Bennink *et al.* showed that photons produced by type-II SPDC can effectively be in a single spatial mode when an appropriately focused pump beam is used, and Ljunggren *et al.* determined the optical focusing condition for maximizing either single or pair coupling efficiency into fibers. This focusing is specified by the parameter $\xi = l/b$, where l is the length of the crystal, and $b = 2z_R = 2n\pi w_0^2/\lambda$ is the confocal parameter of a Gaussian beam with beam waist w_0 in a medium with index of refraction n. The optimal focusing parameter ξ for collinear emission of signal and idler photons ranges between 0.5 and 1.5 for the pump beam. We optimize this coupling efficiency by adjusting the pump focus around $\xi \approx 1$ and varying the corresponding fiber coupling parameters for signal and idler photons.

In our experiment, this mode matching condition equates to choosing a focusing beam waist such that the confocal parameter is roughly equal to the length of the crystal adjusted for index of refraction. In our experiment, we choose the free-space confocal parameter

$$b = 2z_R = \frac{2\pi w_0^2}{\lambda} = \frac{L}{n} \tag{2.16}$$

which yields the beam waist

$$w_0 = \sqrt{\frac{\lambda L}{2\pi n}}. \tag{2.17}$$

2.5 Summary

We have just summarized several fundamental concepts for understanding efficient second-order nonlinear processes, particularly SPDC, the experimental focus of this thesis. In the next chapter, we apply our discussion of quasi-phase matching and pump focusing to characterize a PPLN crystal for SPDC output and its fiber coupling.

Chapter 3

Experimental Design and Results

In this chapter, we discuss the verification of quasi-phase matching in PPLN and the single-photon characterization of SPDC from a pump beam at 532 nm. After describing the experimental configuration for difference frequency generation and lock-in photodetection, we characterized our PPLN sample in a series of steps:

1. First, we verified its poling period, effective length, and focusing parameter by comparing the phase matching bandwidth predicted by the crystal's Sellmeier equation to the measured value. Using the effective crystal length in a theoretical model of phase matching and temperature bandwidths should closely match with experiment.

2. Second, we verified the effective nonlinear coefficient d_{eff} by measuring the signal power in a DFG measurement.

3. Third, we coupled the signal and idler beams into single-mode optical fibers, characterized the efficiency of SPDC at the signal and idler wavelengths, and carried out coincidence counting. By measuring the systems transmission efficiencies of our experimental setup, we can determine the probability of idler photon arrivals conditional on the detection of the corresponding signal photon.

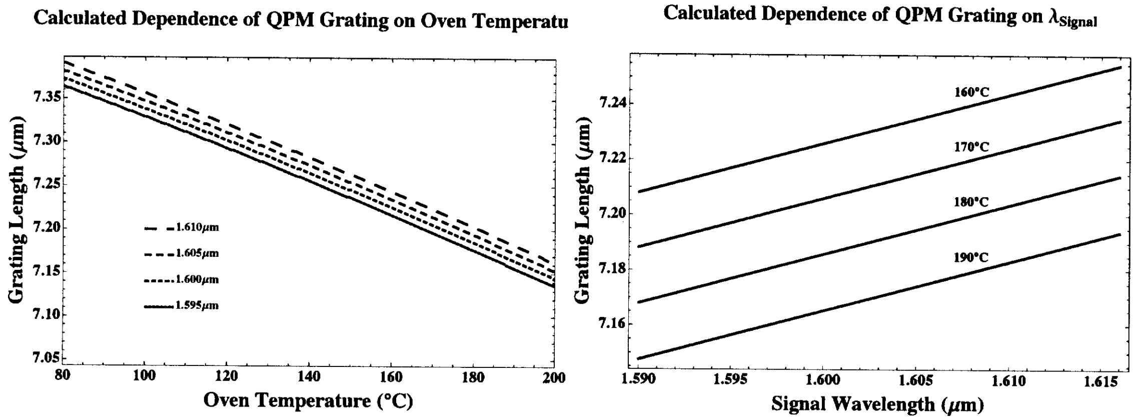

(a) Dependence of phase matching bandwidth on effective length of crystal nonlinearity.

(b) Dependence of temperature bandwidth on effective length of crystal nonlinearity.

Figure 3-1: Temperature and wavelength tuning behavior for quasi-phase matching. By choosing a correct temperature and grating, we can achieve quasi-phase matching by tuning signal wavelength.

Coefficient	1	2	3	4	5	6
A_{1-6}	5.35583	0.100473	0.20692	100	11.34927	0.015334
B_{1-4}	4.6290×10^{-7}	3.8620×10^{-8}	-8.90×10^{-9}	2.657×10^{-5}		
α, β	1.54×10^{-5}	5.3×10^{-9}				

Table 3.1: Sellmeier and thermal expansion coefficients for 20mm PPLN crystal sample .

3.1 Experimental Setup for Difference Frequency Conversion

Before proceeding with our SPDC experiment, we first characterized our PPLN crystal at the operating wavelengths using DFG of $\sim$ 800nm light from a strong pump beam at 532 nm and a weak probe beam tunable between 1590 – 1620 nm. We used an HC Photonics Corp congruent PPLN crystal measuring 20(L)×5.3(W)×5(H)mm^3 and antireflection-coated (AR) at three wavelengths (532 nm, 800 nm, and 1550 nm). The crystal contained five equally-spaced channels with grating periods ranging from 6.9 to 7.3 μm. Because we employed a type-0 phase matching process, all polarizations aligned parallel to the crystal's optical z-axis. We are subsequently interested in calculating the extraordinary index of refraction n_e at the pump, signal, and idler

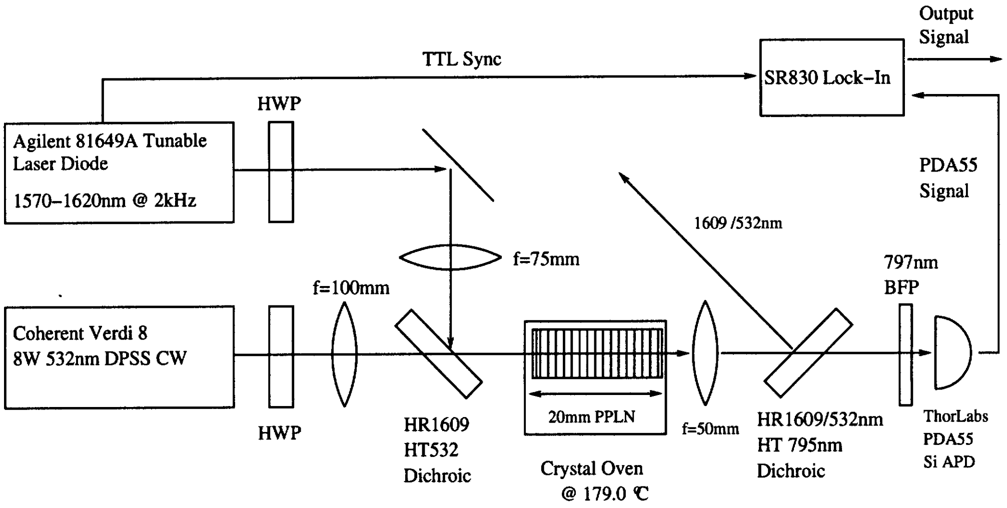
Output Signal
TTL Sync
SR830 Lock-In
HWP
Agilent 81649A Tunable Laser Diode
1570–1620nm @ 2kHz
PDA55 Signal
1609 /532nm
f=75mm
797nm BFP
f=100mm
Coherent Verdi 8
8W 532nm DPSS CW
HWP
HR1609 HT532 Dichroic
20mm PPLN
Crystal Oven @ 179.0 °C
f=50mm
HR1609/532nm HT 795nm Dichroic
ThorLabs PDA55 Si APD

Figure 3-2: Schematic difference frequency generation setup.

wavelengths. An experimentally-determined Sellmeier equation describing its wavelength and temperature dependence (in °C) is provided by the manufacturer,

$$n_e^2(\lambda, T) = A_1 + B_1 f + \frac{A_2 + B_2 f}{\lambda^2 - (A_3 + B_3 f)^2} + \frac{A_4 + B_4 f}{\lambda^2 - A_5^2} - A_6 \lambda^2 \tag{3.1}$$

where

$$f(T) = (T - 23.5)(T + 23.5 + 546). \tag{3.2}$$

The Sellmeier coeffcients for this expression are listed in Table 3.1.

The Sellmeier equation is used to calculate the poling period necessary to satisfy the quasi-phase matching condition given in Equation 2.11. Note that we must also account for the physical expansion of crystal and the lengthening of the poling period at the operating temperature such that

$$\Lambda(T) = \frac{\Lambda_0}{1 + \alpha(T - 25) + \beta(T - 25)^2}, \tag{3.3}$$

where thermal expansion coefficients α and β are given in Table 3.1. A QPM channel in the crystal was chosen by estimating the required grating period needed for phase matching in certain wavelength and temperature ranges. Figure 3-1 shows sample grating periods generated over the temperature range of the commercial Super Optronics crystal oven and wavelength range of the 1.6 μm source (Agilent 81649A). Figure 3-1(b) shows that grating periods smaller than 7.2 μm will likely be outside the range of the crystal oven. Subsequently, the 7.2 μm grating was chosen as it allowed for potential QPM to occur comfortably within the range of the signal source and crystal temperature.

The schematic for our DFG measurement is shown in Figure 3-2. To provide a single-mode, linearly polarized pump source, the light from a Coherent 8W Verdi pump laser at 532 nm was attenuated from a stable output power of 4.0 W to 40 mW using two dichoic mirrors transmitting only 10% at 532 nm. The beam was coupled into a single-mode, polarization maintaining (PM) optical fiber with efficiency of nearly 75% using a Nikon microscope objective (f = 11.0 mm). The input signal source was an Agilent 81649A compact laser module tunable between 1590 and 1620 nm. Pump and probe beams were collimated using microscope objectives, passed through HWPs to ensure parallel polarization, and then combined using a dichroic mirror to ensure collinear propagation along the crystal x-axis. After the pump and probe beams were collinearly aligned over approximately two meters, two AR-coated BK7 lenses were added to focus the beams down to approximately diameters of 54 μm and 96 μm, respectively, as measured directly using a Photon, Inc. BeamScan scanning-slit profiler. Overlap of the two focused beams was checked and a final alignment was made to ensure collinear propagation through the crystal. Once the beams were mode matched, the temperature-stabilized PPLN sample was placed in the beam path and centered, a dual-wavelength AR-coated collimating lens was placed at the output, and a dichroic mirror reflecting 1550 nm but passing 800 nm and some 532 nm was added to filter the separate input and output beams. To ensure flexibility of alignment for mode matching, the focusing lens, collimating lens, and insulated crystal oven were mounted on ThorLabs linear translation stages.

The DFG process was initially very weak, and we employed a lock-in detection scheme using a variable gain Si ThorLabs PDA55 photodiode and a Stanford Research Systems SR830 lock-in amplifier. The signal source was internally modulated at 2 kHz, and TTL synchronization pulses from the Agilent 81649A module clocked the lock-in amplifier. Adjusting the height of the crystal in the beam path, we tried phase matching for each grating over the temperature and wavelength ranges appropriate for the 7.2 μm grating, while observing the lock-in signal. A signal voltage was observed at 179.0°C, and the probe wavelength was adjusted to 1604.7 nm to maximize the output signal and hence achieve phase matching. Crystal position, focusing, and beam alignment were varied until the output power was maximized.

3.2 Phase Matching Bandwidth

The manufacture of periodically poled crystals is prone to fabrication error, such as finite error in grating spacing, missed inversions, and random error in the position of grating boundaries [FMJB92]. Quasi-phase matching, therefore may not occur over the entire physical length of the crystal. Our goal in this section is to use the crystal's measured phase matching bandwidth to determine the effective length over which quasi-phase matching actually occurs.

First, to verify the DFG output, we used the measured power from lock-in photodetection to determine the phase matching bandwidth of our crystal. The measured output power from the lock-in is given by

$$P_s = \frac{V_s}{G \times \eta_{\lambda_s}}, \tag{3.4}$$

where V_i is the observed lock-in voltage from the PDA55 photodiode, G is the transimpedance gain (1.5×10^4V/A), and η is the detector responsivity (0.55 for 797 nm). After the alignment procedure of the previous section, the phase matching bandwidth was measured by recording the output voltage as a function of the input signal power at a fixed crystal temperature. Temperature bandwidth measurements were accomplished similarly by varying the crystal temperature at a fixed wavelength of 1604.7 nm. The DFG output of an 8 mW pump beam modulated by a 1.90 mW probe beam (50% duty cycle at 2kHz) at 1604.7 nm was approximately 510 nW, as measured by the lock-in and a Coherent FieldMaster power meter.

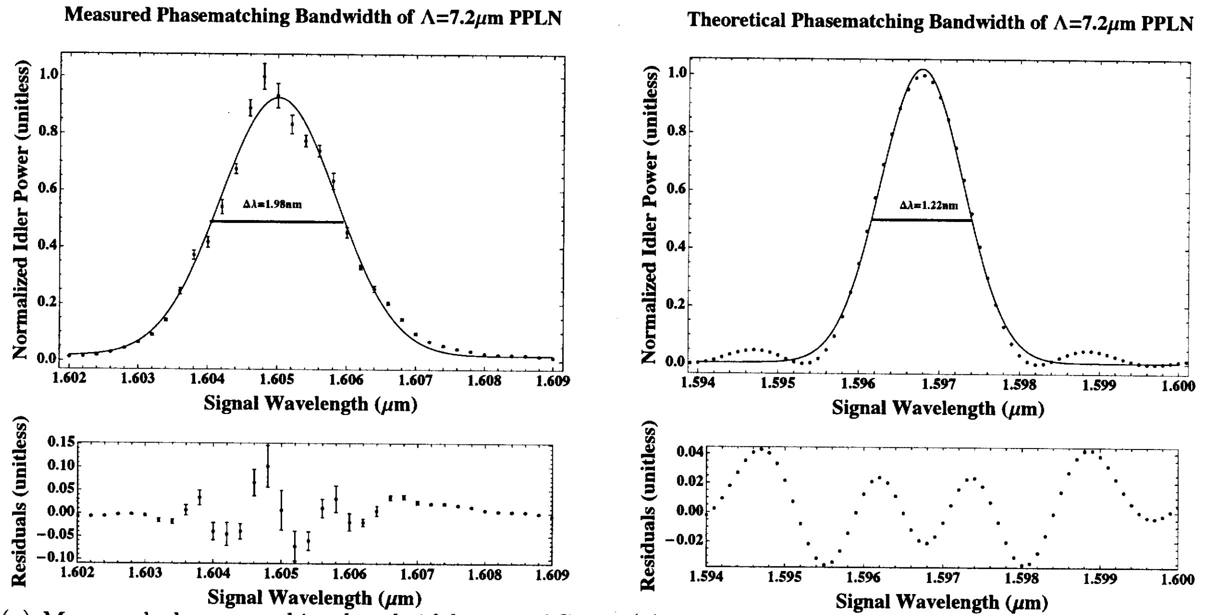

(a) Measured phase matching bandwidth at 179°C.

(b) Theoretical phase matching bandwidth at 179°C for a 20 mm PPLN crystal.

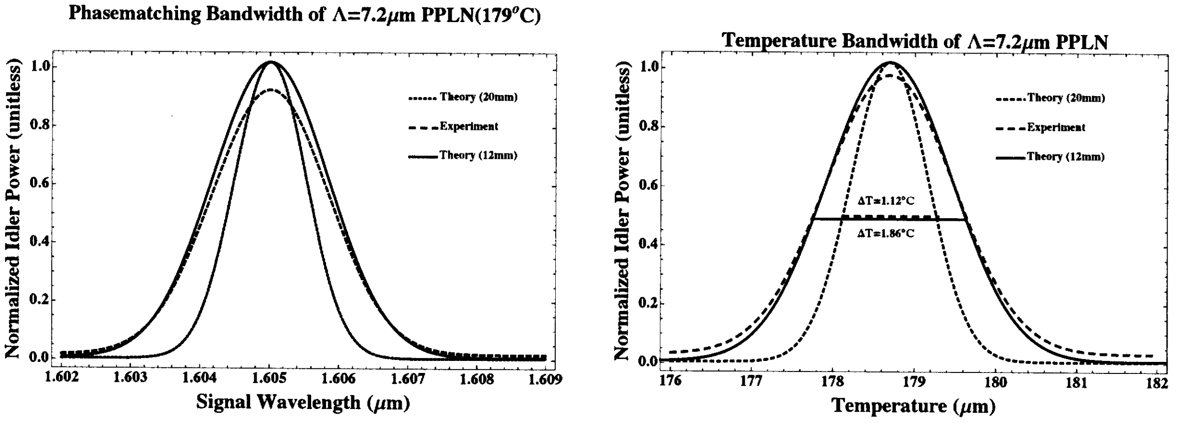

(c) Dependence of phase matching bandwidth on effective length of crystal nonlinearity.

(d) Dependence of temperature bandwidth on effective length of crystal nonlinearity.

Figure 3-3: Phasematching and temperature bandwidth measurement and theory for 7.2 μm grating in 20 mm PPLN crystal. Figures 3-3(a) and 3-3(b) show experimental and generated phase matching curves for PPLN, their Gaussian fits, and the residuals. Comparing their fits, we see that a shorter effective crystal length is required to explain experimental phase matching and temperature bandwidths.

Figure 3-3 shows normalized experimental and theoretical phase matching curves for wavelength and temperature. Theoretical phase matching and temperature bandwidth curves for a 20 mm PPLN crystal were generated numerically using Equation 3.1 in an Microsoft Excel spreadsheet provided by the HC Photonics. Theoretical and experimental data were fit using the Lev Marquandt nonlinear fitting algorithm in Mathematica 6. However, as this package was unable to handle the singularities of the sinc function, we have approximated the data using normalized Gaussians with a constant background. The residuals from the experimental fit in Figure 3-3(a) deviate significantly at the tails, clearly not accounting for the side lobes expected in a phase matching measurement. Smaller deviations are found at the mean and within the full-width half maximum of the curve. These features are consistent with the residuals from the theoretical data shown in Figure 3-3(b), and we therefore use the data extrapolated from our measurement to determine the phase matching bandwidth. For a Gaussian fit with standard deviation σ, we define the phase matching bandwidth as the full width at half-maximum given by $\sigma\sqrt{2\ln 2}$.

Applying the phase matching condition in Equation 2.9 to this phase matching bandwidth definition, we find the phase matching bandwidth to be 1.98 nm, compared to 1.22 nm in the theoretical case estimate. The larger bandwidth suggests a shorter effective length than the physical length of the crystal (20 mm). Applying the phase matching bandwidth condition, we find that the effective length is $l = 12.37$ mm. Subsequently, we see in Figure 3-3(c) that the calculated phase matching is much closer to experimental value using this effective length. A similar discrepancy occurs between experiment and calculated temperature bandwidth (1.12°C) at 20 mm, as shown in Figure 3-3(d), where a re-calculated temperature tuning curve with $l = 12.37$ mm better approximates the measured 1.86°C temperature bandwidth.

3.3 Effective Nonlinear Coefficient

The remaining task in characterizing the PPLN crystal was to measure its effective nonlinear coefficient d_{eff}. Although an ideal quasi-phase matched PPLN has $d_{\text{eff}} =$

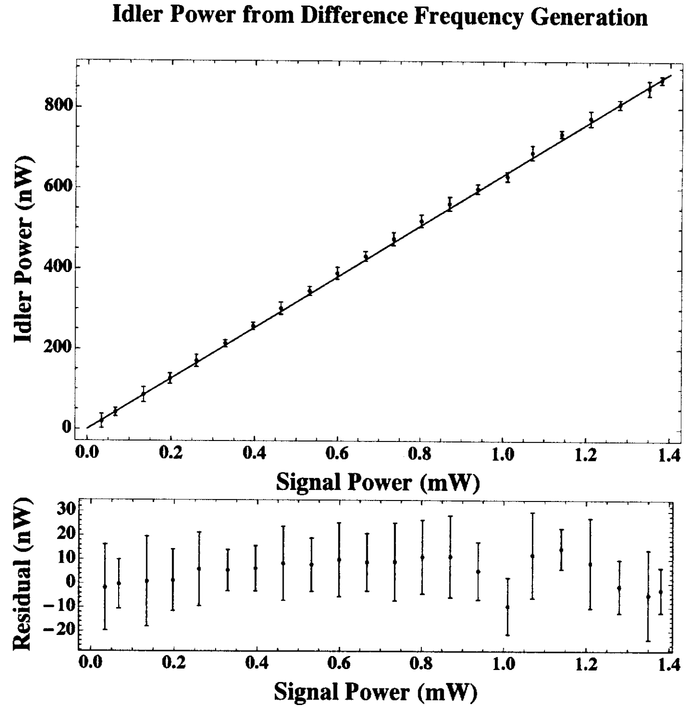

Figure 3-4: Linear dependence of difference frequency generation at 797 nm on signal power 1.6 μm at 532 nm fixed pump.

$2d_{33}/\pi \approx 17.3$ pm/V [RSW], we expect a smaller value for our sample. The output idler power P_s from a DFG process [CBCT92] is given by

$$P_s = \frac{16\pi d_{\text{eff}}^2 P_p P_i l \bar{h}_m\left(B,\xi\right)}{c\epsilon_0 n_p n_s n_i \lambda_i^2 \left(\frac{1}{k_p}+\frac{1}{k_s}\right)} \text{sinc}^2\left(\frac{\Delta k l}{2}\right). \tag{3.5}$$

For a wavelength λ, the experimental parameters in this expression are all specified for an extraordinary refractive index $n_e\left(\lambda\right)$, calculated from Equation 3.1. For each wave, the wave vectors and confocal beam parameter are $k = 2\pi n_e/\lambda$ and $b = 2\pi n_e w_0^2/\lambda$, respectively, and the focusing parameter is $\xi = 0.96$ for a pump beam diameter of 54 μm and physical crystal length of 20 mm. The DFG output occurs over the effective length 12.37 mm. The reduction factor based on the pump beam focusing is $\bar{h}_m = 0.80$ [BK68].

Fixing the input pump power (2.29 mW) and varying the 1604.7 nm probe power incrementally between 0 and 1.90 mW (50% duty cycle), we measured lock-in voltages and obtained the output powers according to Equation 3.4. When fitting to this data, we assume theoretical values of the index of refraction using the Sellmeier equation in Equation 3.1. The plot of the resulting data is shown in Figure 3-4, following the expected linear dependence of signal power on probe power given in Equation 3.5. A least squares fit in Mathematica yields a nonlinear coefficient $d_{\text{eff}} = 2d_{33}/\pi \approx 12.5$ pm/V.

3.4 SPDC Flux of Single Photons

To carry out coincidence counting of the downconversion output, we must first couple the idler and signal photons into their respective single-mode optical fibers. Our goal in this section is to use our DFG output (796 nm) and residual pump (532 nm) and probe (1.6 μm) beams to achieve this coupling. The single-mode DFG output will couple more efficiently into the fiber than the multi-mode SPDC output, and will therefore be only an approximation of SPDC coupling efficiency.

We first removed the filtering dichroic mirror from the residual pump beam used in the difference frequency conversion, and partially couple the pump into the 796 nm signal fiber using a 4.5 mm collimating lens. Exploiting the collinearity of the pump and signal photons, we then optimized the coupling of the signal photons to the fiber using lock-in photodetection. Reinstalling the dichroic mirror into the setup, the mirror reflected the 1.6 μm probe beam and almost 90% of the residual pump power. We coupled the residual 1.6 μm probe photons into a single mode fiber, and placed a 797 ± 1.5 nm bandpass interference filter in the signal path to filter out any remaining pump photons. We measured coupling efficiencies of 60% and 70% through the signal and idler fibers, respectively.

The signal and idler photons were measured using a fiber-coupled Perkin-Elmer silicon photon counting module (SPCM-AQRH-13) and an InGaAs avalanche photodiode (APD), each connected to a National Instruments LabView data acquisition board and coincidence counting circuit. The quantum efficiency at 797 nm is taken to be 52% with an active quenching dead time of 32 ns. Without any input fiber, the Si APD measured a dark count rate of 250 Hz (counts/sec), consistent with the datasheet specification. The InGaAs APD was thermoelectrically cooled to −25°C at a bias voltage 50.36 V, and was used in Geiger mode triggering off of a SRS DG535 delay/pulse generator. The InGaAs detectors quantum efficiency was 12% and dark counts on the order of 17 kHz were measured in the absence of a source.

By measuring losses in our SDPC setup, we can determine the expected production of photon pairs. Photons are generated at a rate R. The Si and InGaAs SPCMs have quantum efficiencies given by η_{Vis} and η_{IR}, respectively, and we also have empirical losses η_s (signal) and η_i (idler) that account for reflection losses from beamsplitters, bandpass filters, and coupling efficiency into single-mode optical fiber. The number of signal and idler photons detected are $S_s = \eta_s \eta_{\mathrm{Vis}} R$ and $S_i = \eta_i \eta_{\mathrm{IR}} R$, respectively. The number of coincidences detected is then given by $C = \eta_{\mathrm{IR}} \eta_{\mathrm{Vis}} \eta_s \eta_i R$.

For our experiment, the SPCM counting efficiencies were $\eta_{\mathrm{IR}} = 0.15$ and $\eta_{\mathrm{Vis}} = 0.52$. Optical inefficiencies in the signal and idler paths account for the transmission and reflection of the filter dichroic mirror at the output, the near-IR bandpass filter, dielectric mirrors used for alignment, the fiber collimators, and the AR coating at the fiber tip. These transmissions are directly measured using a laser power meter or lock-in voltages. The aggregated system transmission inefficiencies are given by,

$$\begin{aligned} \eta_i &= 0.4 \text{ (transmission)} \times 0.6 \text{ (coupling)} \approx 0.24 \\ \eta_s &= 0.6 \text{ (transmission)} \times 0.7 \text{ (coupling)} \approx 0.42, \end{aligned} \tag{3.6}$$

and the resulting probability of simultaneous arrival is

$$C/R = \eta_{\mathrm{IR}} \eta_{\mathrm{Vis}} \eta_s \eta_i = 0.15 \times 0.52 \times 0.42 \times 0.24 \approx 0.008. \tag{3.7}$$

The expected spectral brightness is given by Byer and Harris [BH68], for a crystal of length l, pump power P_p, and solid angle of emission θ (in radians):

$$P_i = \beta l^2 P_p \int_{-\infty}^{\infty} \int_0^{\theta} \mathrm{sinc}^2\left(\frac{\Delta k l}{2}\right) \phi \mathrm{d}\phi \mathrm{d}\omega \tag{3.8}$$

where

$$\beta = \frac{2d_{\text{eff}}^2 \hbar n_i}{(2\pi)^2 \epsilon_0^3 \lambda_i^4 \lambda_s n_s n_p}. \tag{3.9}$$

For small divergence angles, the phase mismatch Δk can be approximated in terms of frequency and angular dispersion constants b (empirically 6.1×10^{-10} s/m) and $g = k_p k_i / 2k_s$ such that

$$P_i = \beta l^2 P_p \int_{-\infty}^{\infty} \int_0^{\theta} \operatorname{sinc}^2 \left[\left(b\omega - g\phi^2 \right) \frac{l}{2} \right] \phi \mathrm{d}\phi \mathrm{d}\omega, \tag{3.10}$$

which can be integrated to yield

$$P_i = \frac{\beta l P_p}{b} \pi \theta^2. \tag{3.11}$$

At a solid angle $\theta = 10$ mrad and pump power $P_p = 7.92$ mW, Equation 3.9 yields an expected idler count of rate of 9.8×10^6 Hz, consistent with the measured value $R_i = 1.1 \times 10^7$ Hz and just under the saturation region of the Si APD. However, pump powers in the mW range can produce multiple coincident pairs, and we subsequently lower the pump power to the μW range. Tuning the crystal oven 10°C off resonance, we found that the pump photons reaching the Si APD were on the order of the dark counts. Incrementally reducing pump power from 30 μW to 1 μW and recording single counts, we have shown in Figure 3-5(a) that the number of detected signal photons has a roughly linear response to input pump power. Applying a least squares fit to this data, we find a measured signal flux of 5.18×10^5 Hz/mW.

The remaining parameter for determining spectral brightness is given by the SPDC phase matching bandwidth. The sinc^2 function in the integrand of Equation 3.10 drops to 1/2 at $\Delta k \approx 0.886\pi/2l$, and from this it can be shown that the SPDC phase matching bandwidth (in frequency) is given by

$$\Delta f = \frac{g}{2\pi b} \theta^2, \tag{3.12}$$

for angles $\theta^2 \sim 2\pi/lg$ [BH68]. This frequency bandwidth can be converted to fre-

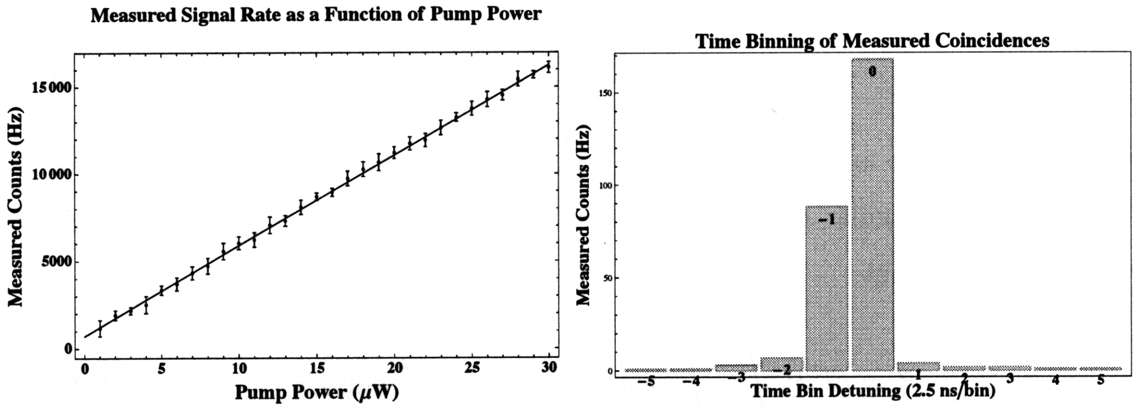

(a) Signal count rates and linear response of an Si SPCM.

(b) Counting rate when detuning from coincidence.

Figure 3-5: Coincidences versus signal-idler time-bin delay.

quency bandwidth, as $\Delta\lambda = \lambda^2 \Delta f / c$. Applying the wavelengths for the DFG from Section 3.3 and the effective crystal length from Section 3.2, we determine the phase matching bandwidth to be 1.44 nm. This value is consistent with the values determined numerically and experimentally in Section 3.3. Accounting for this bandwidth, we find that the measured spectral brightness of our SPDC source is 3.6×10^5 Hz/mW/nm for the idler wavelength at 1.6 μm.

3.5 Coincidence Counting in a Single-Pass Measurement

In this section, we combine our measurement of SPDC flux in Section 3.4 with coincidence counting to determine the probability of idler photon detection conditional on the signal photon detection. The setup for coincident counting is shown in the block diagram in Figure 3-6. After optimizing alignment, the signal photons at 797 nm were detected using a Si APD and the 1.6 μm idler photons were detected using a fiber-coupled InGaAs APD.

We perform coincidence counting by using the arrival of the signal photon at the Si APD to trigger the bias gate for the InGaAs APD. We employed a DG535 gate and delay generator to trigger the InGaAs APD and introduced a variable time delay

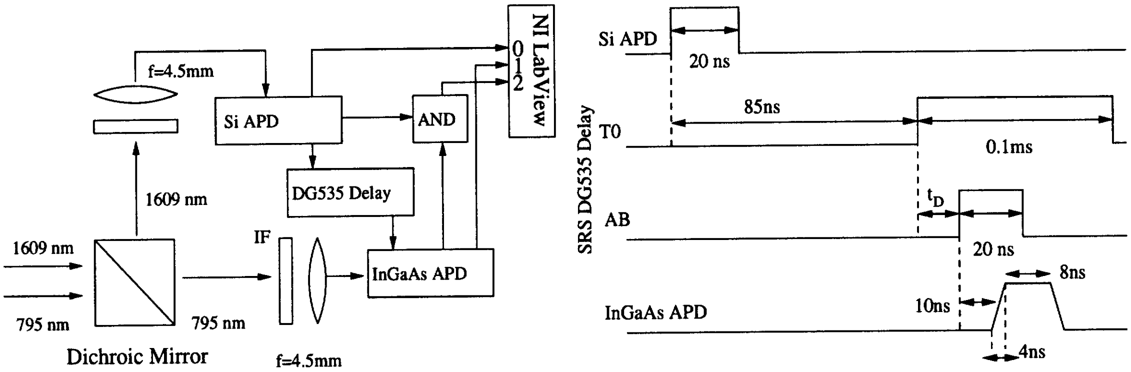

(a) Setup for fiber-coupled coincidence counting.

(b) Timing diagram.

Figure 3-6: Conditional coincidence counting of idler photons.

t_D allowing coincident gating of signal and idler photon pairs. The relevant times for controlling the DG535 are shown in Figure 3-6(b). The arrival of a signal photon at the Si APD generated a 20 ns-wide TTL pulse which was split three ways to the DG535, the coincidence counter, and the LabView acquisition card. The length of the coax cable at the coincidence detector and the DG535's internal delay contributed a fixed delay of 85 ns. To limit after-pulsing in the InGaAs APD, the clock pulse T_0 of the delay generator was set at a maximum detection rate of 50 kHz during which triggers from signal photon arrivals were ignored. An additional delay of 10 ns was added before the InGaAs APD could indicate the arrival of a idler photon with a 8-ns-wide TTL pulse. The resolution of the coincidence counter and the LabView acquisition card limited our coincidence window to 2.5 ns time bins.

Pumping the crystal at approximately 30 μW, we collected downconverted photons and detected signal photons at a rate of almost 17,000 Hz. Varying the time delay over a wide range and counting coincidences in bins of 2.5 ns, we find a maximum number of coincidences at a time delay of approximately 340 ns. The number of coincident photons is found by summing the time bins from Figure 3-5, which amounts to 278 coincidences and a conditional probability of approximately 0.016. Altering the alignment of the fiber collimators for the signal and idler paths did not improve the number of coincidences. To determine the expected coincident probability of arrival, let us define a discrete random variable N, denoting the detection of N photons at a detector. The probability of arrival of a single signal photon at the Si APD is denoted by $P(N_s = 1)$ and the joint probability of arrival at both detectors is $P((N_i = 1) \cap (N_s = 1))$. The expected conditional probability of arrival is then

$$P((N_i = 1) \mid (N_s = 1)) = \frac{P((N_i = 1) \cap (N_s = 1))}{P(N_s = 1)} = \frac{\eta_{\mathrm{IR}} \eta_{\mathrm{Vis}} \eta_s \eta_i}{\eta_{\mathrm{Vis}} \eta_s} = \eta_{\mathrm{IR}} \eta_i. \quad (3.13)$$

Applying the experimental transmission and quantum efficiencies in Section 3.4, the expected conditional probability is 0.0288. The discrepancy between calculated and expected conditional probabilities suggests that our measured coincidences were lower by 45%. This is likely attributed to the spatial mode structure of the SPDC signal and idler photon pairs, which is important even with the use of pump focusing. The multimode spatial mode structure of the SPDC output prevents its coupling from being as efficient as the single-mode coupling from our DFG output, thereby *reducing* the probability that, given the arrival of a signal photon in a single spatial mode, the corresponding *idler photon* is also detected.

Previous work in our group used a 20 mm PPLN crystal with a third-order grating period of 21.6 μm to achieve quasi-phase matched SPDC at the same 0.8 and 1.6 μm wavelengths [MAKW02]. This work inferred a free-space pair generation rate of 1.4×10^7 Hz/s/mW for a probe phase matching bandwidth of 1.26 nm, and pump beam diameter of 180 μm. With a 50% fiber coupling efficiency, they were able to measure a singles rate of 3×10^4 Hz/s/mW at pump powers of 1-2 mW, and inferred a pair generation rate of 1.3×10^5 Hz/mW once fiber coupling and quantum efficiencies were accounted for. Comparing the free-space and fiber coupled efficiencies, we can infer that the collection of a single spatial mode from the multimode output into an optical fiber in this experiment reduced number of collected photons by a factor of a 100. The results from Section 3.4 suggest a dramatic improvement in the percentage of photons we can collect in a single mode by focusing a pump beam to a diameter of 54 μm. Accounting for the signal (21.8%) and idler (1.6%) efficiencies, our inferred generation rate is $1.52 \cdot 10^8$ Hz/s/mW, several orders of magnitude better than that previous work. Part of this improvement (one order of magnitude) was due to our use of a first-order grating PPLN crystal, the remaining being due to the pump focusing configuration. Our measured coincidences is lower, partly because our InGaAs APD may have been lower than expected quantum efficiency.

3.6 Summary

In this chapter, we have summarized our characterization of the nonlinear and phase matching properties of PPLN. Furthermore, we have successfully fiber-coupled SPDC signal and idler photons into single-mode optical fiber by using a focused pump beam, and carried out coincidence counting consistent with the losses of our system.